ACS EARTH AND SPACE CHEMISTRY

http://pubs.acs.org/journal/aesccq

Article

Hydrodynamic Limitations on Biomineralization-Induced Permeability Reduction

Eva M. Albalghiti and Brian R. Ellis*

Cite This: *ACS Earth Space Chem.* 2024, 8, 575−585

Read Online

ACCESS | Metrics & More | Article Recommendations | Supporting Information

ABSTRACT: While the subsurface applications of microbially induced carbonate precipitation (MICP) have so far emphasized near-wellbore permeability reduction, MICP technology may eventually be expanded to support needs as diverse as thief zone remediation in geothermal reservoirs or caprock sealing in CO_2 sequestration sites. For these applications to be realized, however, there is a need to understand whether permeability reduction can be achieved under the high flow velocities that may occur, for example, in zones of locally high permeability or along preferential flow paths. In this study, bioaugmented MICP is applied to three natural limestone cores of similar porosity but differing pore size distribution. The injection strategy includes biomass attachment and growth phases before mineralization, with the goal of separating the effects of each phase on permeability. In order to test the resilience of biomass and precipitate accumulation against flow-induced shear stress, saline solution is injected intermittently at a faster flow rate. Real-time permeability estimates show that biomass accumulation reduces permeability even without mineralization, although biomass accumulation may ultimately be shear-limited. Calcium mass balances suggest that sloughing of precipitates is also possible, though its effect on permeability depends on whether mobilized precipitates induce clogging or are transported out of the core. X-ray computed microtomography imaging of the cores suggests that when flow rates are moderate and preferential flow paths do not dominate flow, precipitates tend to accumulate preferentially in larger pores, yielding controlled, incremental permeability reduction. These findings lay essential groundwork toward refining MICP models to account for spatial heterogeneities in the subsurface.

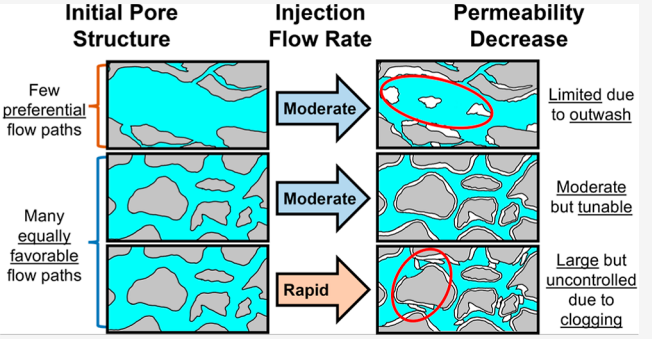

KEYWORDS: *microbially induced carbonate precipitation, biomineralization, reactive transport, permeability, pore size, pore geometry, subsurface*

1. INTRODUCTION

Ureolytic microbially induced carbonate precipitation (MICP) has been studied extensively for over two decades.[1−4] Owing to the low viscosity of MICP reagents, particular interest has emerged around subsurface applications, including immobilization of divalent heavy metals and radionuclides in groundwater,[1,5] as well as trapping enhancement[6] and wellbore leakage mitigation[7−12] at geological CO_2 sequestration sites. Bioaugmentation using *Sporosarcina pasteurii* (*S. pasteurii*) remains the most widely studied MICP approach,[13] though biostimulation of native urease producers has also shown great promise in certain applications.[14−16]

Recent studies have suggested that bioaugmented MICP might also be used for CO_2 leakage mitigation outside the near-wellbore zone,[17,18] relying on the tunability of the injection strategy to influence the quantity and distribution of precipitated carbonate.[19,20] "Continuous-flow" injection strategies are suited to longer-distance transport of reagents due to their ability to counter the natural movement of groundwater.[17] There are, however, trade-offs to these strategies, including near-wellbore clogging and lower overall mineralization efficiency.[19] Near-wellbore clogging may be minimized by using "staged" injection strategies which separate initial biomass accumulation from mineralization rather than injecting microbes and mineralization medium simultaneously.[20] Ultimately, the success of continuous-flow, bioaugmented MICP in natural aquifers hinges on controlling the quantity and distribution of biomass and precipitates along flow paths that may differ greatly in size and geometry.

In porous media, pore size distribution is a key determinant of local flow velocities, which, in turn, mediate the chemical microenvironments and physical forces experienced by both biomass and precipitates during MICP treatment. On the

Received: November 21, 2023
Revised: February 19, 2024
Accepted: February 20, 2024
Published: March 8, 2024

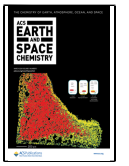

chemical side, the saturation state of the influent medium and the range of Péclet and Damköhler numbers produced by the injection strategy have been well-studied experimentally and incorporated into MICP models at multiple scales.[21−25] On the physical side, the impact of flow velocity on the initial attachment of motile cells[26−28] and the limiting effect of surface shear stress on biomass accumulation[29−31] and biofilm morphology[32−35] are also well-established, albeit outside the specific context of bioaugmented MICP. Some MICP models incorporate shear-induced biomass sloughing by expressing detachment as a function of average flow velocity and biomass quantity.[36] Precipitated carbonates are, in contrast, generally treated as immobile phases, although experimental studies have shown that precipitates are also subject to sloughing and bulk transport.[37] Bulk transport of precipitates was shown to induce feedback loops with local flow velocity whereby certain channels remain open during fracture sealing,[38] implying a limitation on permeability reduction that may be underestimated by current models.

This study assesses the degree to which flow-induced bulk transport of biomass and precipitates can affect permeability reduction in natural porous media subjected to bioaugmented MICP. In contrast to previous experimental investigations of MICP in porous media, which have primarily used unconsolidated columns[20,22,37,39,40] and homogeneous sandstones,[7,41−45] this study uses permeable limestone cores of differing pore size and spatial arrangement. A staged, continuous-flow injection strategy was designed with separate biomass attachment, biofilm cultivation, and mineralization phases, and the impact of each phase on the permeability and effective pore volume was evaluated. Experiments also included eight "intermediate flow" phases where the flow rate was increased either 10- or 30-fold in order to establish an upper bound on the magnitude of flow-induced bulk transport effects. Since acid brine-driven dissolution of precipitates is of concern when MICP is applied to subsurface CO_2 sequestration,[39,44,46] the resilience of permeability reduction to subsequent acid flow was briefly evaluated.

Quantitative and qualitative analyses of both intermediate and post-MICP characterization suggest that while flow-induced shear stresses may have some impact on overall biomass accumulation, the effect on precipitate retention, as well as the relationship between pore size and precipitate accumulation, is more significant here. When flow rates are rapid or preferential flow paths are present, precipitate transport is likely and may inhibit or promote permeability reduction through washout or clogging of pore throats, respectively. In contrast, when flow rates are moderate and flow is distributed evenly across many flow paths, uniform and controlled permeability reduction can be achieved, as precipitates preferentially accumulate in larger pores. These results suggest that flow-induced mobilization of precipitates plays an important role in promoting or limiting permeability reduction and should therefore be considered in field-scale MICP applications. To this end, future studies may further refine MICP models by, for example, clarifying the mechanisms of precipitate mobilization and developing quantitative relationships among pore structure, flow rate, and bulk transport of precipitates.

2. METHODS

2.1. Flowthrough Apparatus. The apparatus used for flowthrough included a high-pressure, temperature-controlled core holder from Core Lab Instruments. Throughout all experiments, the confining pressure and temperature were fixed at 4500 psi and 30 °C, respectively. Viton rubber sleeves were used to isolate the core from the confining fluid and prevent flow at the core boundaries. A total of three Teledyne ISCO high-pressure piston pumps were used; one provided confining pressure to the core holder, while the other two were used alternatingly in flowthrough to eliminate unintentional no-flow periods that would otherwise result from emptying and rinsing the pump between different injection fluids. Two pressure transducers installed at the core holder inlet and outlet recorded the pressure differential every 15 s, enabling permeability estimation in real time using Darcy's law. Prior to flowthrough, cores were vacuum-saturated in Milli-Q water for 12 h. Since Milli-Q water is not in equilibrium with calcite, all water used in both core saturation and injection fluid preparation was pre-equilibrated with crushed Indiana Limestone for at least two weeks and filtered to remove fines immediately prior to use; the sole exception is water used in the growth and mineralization medium (Section 2.4).

2.2. Natural Sample Selection and Preprocessing. Indiana Limestone cores were selected for this study based on several advantageous properties. First, Indiana Limestone is composed of >99% calcite,[47] minimizing the confounding influence of mineralogical heterogeneity on initial bacterial attachment.[48] Second, Indiana Limestone features larger macropores than many homogeneous sandstones (e.g., Berea sandstone), facilitating X-ray computed tomography (XCT) imaging and minimizing the influence of subvoxel porosity on reactive transport processes. Additionally, Indiana Limestone samples are available in a range of initial permeabilities and pore size distributions, and these properties can also be modified in the laboratory via acid flow.

Three Indiana Limestone cores four inches (~101 mm) in length and one inch (~25 mm) in diameter were obtained from Kocurek Hard Rocks Division. Two of these cores had an advertised permeability of 15−30 mD, while the third had an advertised permeability of 0.1−0.5 mD. These cores were designated "HP" ("high-permeability") and "LP" ("low-permeability"), respectively, though it should be noted that these labels are relative—while Indiana Limestones of significantly higher and lower permeability are available, this was the largest permeability range that could be achieved while maintaining similar total porosity across samples.

One of the HP cores was randomly selected to undergo more rapid flow during intermediate flow phases and was therefore designated "HP-RF" ("high permeability-rapid flow"). The LP core was pretreated with flowthrough of hydrochloric acid (pH = 3.0) in order to artificially increase permeability and promote the formation of preferential flow paths.[47,49,50] Acid flowthrough was conducted at the highest flow rate permissible under the pressure limits of the apparatus, ranging from 3 to 60 pore volumes per hour (pv/h). Once permeability began to plateau around 2.5 mD, the core was rinsed with pre-equilibrated Milli-Q water and removed from the apparatus. All cores were dried for 24 h under vacuum with silica gel desiccant and resaturated to estimate total porosity gravimetrically; this was done twice before MICP injection to provide duplicate measurements.

2.3. Core Characterization via XCT. Following gravimetric estimation of bulk porosity, cores were also imaged in 3D using a Nikon μXCT scanner, model XT H 225 ST. This was done both before and after MICP injection. Vacuum-dried

https://doi.org/10.1021/acsearthspacechem.3c00337
ACS Earth Space Chem. 2024, 8, 575−585

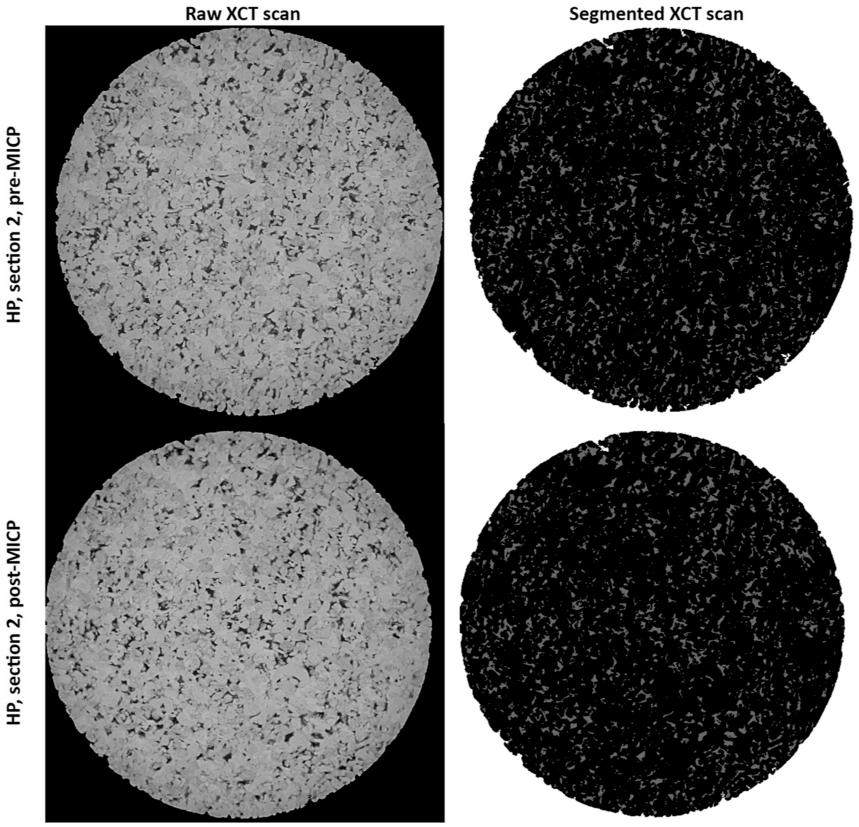

Figure 1. Segmentation of XCT scans demonstrated for an example slice of the HP core, pre- and post-MICP injection.

cores were mounted on the sample stage in 50 mL Falcon tubes with a layer of foam to provide separation from the metal stage, which has a much higher X-ray attenuation coefficient than the cores. The effective pixel size was 15 μm, and the number of projections was optimized to ∼3200, with two frames taken per projection. The exposure time was 1 s for all cores, and the voltage and current ranged from 118 to 127 kV and 119 to 127 μA, respectively, to optimize the histogram of grayscale values (Table S1). Ring artifacts were minimized by bringing the sample stage to a stop between projections. During reconstruction, the center of rotation was calculated automatically, and a beam hardening filter was applied. Reconstructed images were exported as TIFF stacks for further analyses. Four scans were necessary to capture the full length of each core, and scans were set to overlap by 3.75 mm (250 slices) on either end to allow aligning of image stacks and ensure that grayscale values remained consistent across scans; this also allowed the top and bottom 175 slices, which contained visible beam hardening artifacts, to be removed during reconstruction. The core sections captured by each scan are labeled #1−4, with Section 1 being adjacent to the core holder inlet and Section 4 being adjacent to the outlet during MICP injections.

Manual inspection of the scans confirmed that all scans were of good quality, and the grayscale-value histogram of macropores did not overlap with that of solid matrix. Therefore, segmentation of cores into pore and solid space was accomplished through autothresholding in ImageJ. For two example image stacks, the resulting segmented stack was compared to one prepared through the optimized, but more time-consuming, protocol described by Thompson et al.[51] to confirm that the segmentations were comparable. Example raw and segmented images for the HP core are shown in Figure 1.

The porosity of each core section was estimated directly from the histogram of the corresponding segmented stack. Subsequently, the pixels corresponding to the pore space were extracted from each segmented stack, and ImageJ's "Analyze Particles" feature was used to estimate the size distribution of XCT-resolved macropores. For pre-MICP scans, the distribution was divided into 50 bins of increasing pore size with each bin corresponding to 2% of the total XCT-resolved pore volume. The preferential localization of precipitates within pores of different sizes was then analyzed by separating post-MICP porosity into the same bins and calculating the percent change in porosity within each bin.

2.4. Injection Strategy. *2.4.1. Inoculum Preparation.* *S. pasteurii* (ATCC 11859) was initially resuscitated from its freeze-dried shipping state in a liquid growth medium containing the equivalent of 3 g/L Difco nutrient broth (prepared in the laboratory from beef extract and potato peptone) with 0.15 M ammonium chloride and 0.3 M urea. The growth medium was sterilized by vacuum filtration through 0.2 μm bottle-top filters into 1 L autoclave-sterilized glass bottles; filter-sterilization was used to prevent urea volatilization in the autoclave.

250 mL cultures were incubated in 500 mL autoclaved Erlenmeyer flasks with open-cell foam stoppers at 30 °C for 48 h, shaken at 90 rpm. Following this initial resuscitation, 1 mL of culture was transferred to 250 mL of fresh medium and incubated for 18 h to an OD600 of ∼0.6. A final culture was inoculated according to the same procedure and grown for 12 h to an OD600 of ∼0.4. This culture was pelleted in 50 mL sterile centrifuge tubes at 4500 rpm for 15 min before

https://doi.org/10.1021/acsearthspacechem.3c00337
ACS Earth Space Chem. 2024, 8, 575−585

Table 1. Summary of the Applied Injection Strategy

phase	influent chemistry	volume (pore volumes)	flow rate (pv/h)	no-flow pause (h)
pre-sterilization[a]	70% ethanol/30% Milli-Q water[b]	10	30	1
intermediate flow 1	0.9% sodium chloride[b]	15	3, 5, 10, 15, 30, (60, 90)[c]	0
	4% potassium chloride[b]			
	0.9% sodium chloride[b]			
attachment	0.9% sodium chloride[b] with suspended *S. pasteurii*, OD600 = 0.1, pH = 8.3	6	3	0
intermediate flow 2	*(same as intermediate flow 1)*			
growth 1	3 g/L Difco nutrient broth, 0.3 M urea,0.15 M ammonium chloride, pH = 6.5	12	1	0
	0.9% sodium chloride[b]	5	30	0
	3 g/L Difco nutrient broth, 0.3 Murea, 0.15 M ammonium chloride, pH = 6.5	12	1	0
intermediate flow 3	*(same as intermediate flow 1)*			12
growth 2	*(same as growth 1)*			
intermediate flow 4	*(same as intermediate flow 1)*			12
mineralization 1	3 g/L Difco nutrient broth, 0.3 M urea, 0.15 M ammonium chloride, 0.3 M calcium chloride dihydrate, pH = 6.0	6	3	0
	(same as above)	6	30	0
intermediate flow 5	*(same as intermediate flow 1)*			
mineralization 2	*(same as mineralization 1)*			
intermediate flow 6	*(same as intermediate flow 1)*			12
mineralization 3	*(same as mineralization 1)*			
intermediate flow 7	*(same as intermediate flow 1)*			
mineralization 4	*(same as mineralization 1)*			
intermediate flow 8	*(same as intermediate flow 1)*			
	break: vacuum drying, XCT characterization, and re-saturation in Milli-Q water[b]			
acid flow	hydrochloric acid, pH = 3.0	125	1, 3, 10, 15, 30, 60, 90 (highest possible)	0

[a]Expected to remove active cells but not endospores. [b]Pre-equilibrated with Indiana Limestone. [c]60 and 90 pv/h for the HP-RF sample only.

decanting the medium and re-suspending the pellet in 0.9% sodium chloride. This was repeated to remove excess growth medium, and the resulting cell suspensions were stored short-term at 4 °C for up to 2 weeks. 0.9% sodium chloride was used to reduce the osmotic pressure on cells associated with Milli-Q water exposure. As with all injected fluids excluding the growth and mineralization medium, the sodium chloride solution was pre-equilibrated with Indiana Limestone prior to filter-sterilization, resulting in a pH of ∼8.3.

36 h before a scheduled injection, a 50 mL short-term storage suspension was removed from refrigeration and 1 mL was used to inoculate a 250 mL culture. After 12 h of incubation, a new culture was inoculated with 1 mL of the previous culture and grown for 12 h to ensure that an OD600 of 0.40 was reached. Cells were then rinsed and re-suspended in 0.9% sodium chloride according to the procedure above, then diluted to a final OD600 of 0.10 and stored for 12 h at 4 °C prior to starting the injection.

2.4.2. MICP Injection. The sequence of injection steps is summarized in Table 1, with additional details and rationale for the injection strategy design discussed here. Prior to MICP injection, the internal temperature of the core holder was brought to 30 °C and a confining pressure of 4500 psi was applied; these values remained fixed for the duration of the injection. Ten pore volumes (10 pv) of 70% ethanol solution were injected followed by a no-flow period of 1 h to eliminate any living cells within the core, after which, the core was flushed with 10 pv of sterile 0.9% sodium chloride solution. Injections began with the first of eight intermediate flow phases, where permeability was estimated at flow rates ranging from 3 to 30 pv/h or up to 90 pv/h in the case of the HP-RF sample. Two tracer tests were also conducted at 30 pv/h to estimate the effective pore volume available for flow.

During the "attachment" phase, 6 pv of cell suspension was injected at a flow rate of 3 pv/h. The absence of the growth medium during attachment was meant to ensure that the fraction of injected biomass initially retained was consistent across samples and could be reliably estimated based on influent and effluent OD600 (Table S2). Since the OD600 was not calibrated to cell number using plating-based or total protein assays, optical density values reported here are used only for internal comparison between the three experiments. It is also important to note that some biomass flocculation could occur, even at the relatively low ionic strength and OD600 used here. Since the only purpose of the attachment phase was to ensure the presence of *S. pasteurii* within the cores, the prevalence and size of flocs was not assessed.

Following the attachment phase, intermediate flow was repeated, and the first "growth" phase was initiated immediately after rinsing the piston pump and upstream lines with 70% ethanol and 0.9% sodium chloride. 12 pv of growth medium was injected at a flow rate of 1 pv/h; preliminary experiments suggested that this was the longest residence time at which the effluent medium could still support

https://doi.org/10.1021/acsearthspacechem.3c00337
ACS Earth Space Chem. 2024, 8, 575−585

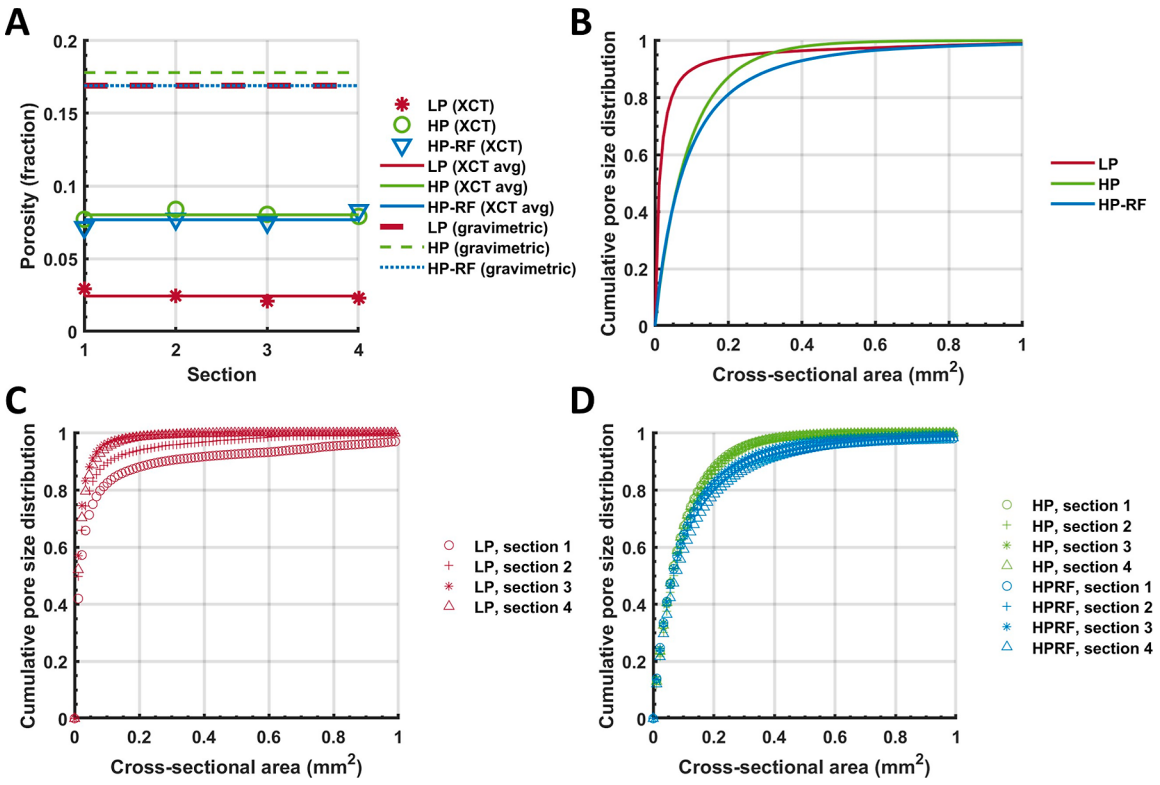

Figure 2. Characterization of initial (A) core porosity and (B–D) pore size distribution, obtained via XCT and gravimetric methods. Only pores larger than ∼15 μm in diameter are captured by XCT, which accounts for ∼45% of gravimetrically determined porosity in HP and HP-RF and ∼14% in LP.

significant biomass growth, implying that growth would occur along the entire length of the core. At the 6 h mark, piston pumps were switched and the previously used pump was cleaned. This was done to minimize bacteria migration and colonization of the influent medium, which would effectively increase the growth medium residence time and shift the mechanism of biomass accumulation to the attachment of influent suspended cells. As evidenced by elevated pH and OD600 in the upstream lines at the end of each growth phase, however, this was not entirely successful (Table S2). At the end of the first growth phase, intermediate flow was performed, and the core was left saturated with 0.9% sodium chloride for 12 h overnight. On the next day, a second growth phase was carried out according to the same procedure as for the first.

Four "mineralization" phases were carried out, with intermediate flow phases immediately following each. A moderate flow rate of 3 pv/h was used to prevent the complete depletion within the core, thereby promoting more homogeneous precipitation along the flow path. This flow rate was maintained for 2 h, followed immediately by flushing an additional 6 pv at a higher flow rate of 30 pv/h. The purpose of flushing was to ensure that all the effluent medium was collected for dissolved calcium analysis, and unadhered precipitate colloids were removed prior to the next intermediate flow phase. Following post-MICP characterization of cores, an acid flow test was conducted on each, following a method similar to that applied during predissolution of the LP core.

Reynolds (Re) and Péclet (Pe) numbers were estimated for the intermediate flow and mineralization phases, respectively (Table S3), in order to verify that flow remained in the laminar regime and that mass transport was diffusion-limited. Since neither the maximum pore-scale velocity nor the average pore diameter could be determined directly, a range of estimates were computed for each core based on the size distribution of XCT-resolved macropores.

2.5. Tracer Test Analysis. Conservative tracer tests are one method of estimating the mean hydraulic residence time (MHRT or $\overline{t}$) and effective pore volume within a porous medium.[52,53] When the effluent concentration is normalized to the maximum concentration, the step-input tracer method employed here yields the cumulative residence time distribution, $F(t)$, or the integral of the exit curve $E(t)$. The standard approximation of $\overline{t}$ from $F(t)$[54] is modified to use units of pore volumes, V, in place of time units; this yields the following estimation of effective pore volume, V_{eff}

$$V_{\text{eff}} = \int_0^1 V \, dF(V) \approx \sum_{\text{all } i} \left[\left(\frac{V_i + V_{i-1}}{2} \right) (F(V_i) - F(V_{i-1})) \right] \quad (1)$$

Since V is normalized to the gravimetrically estimated pore volume of each core, it follows that a V_{eff} equal to one would be expected when all pore space is equally available to flow. This metric is therefore used to identify trends in the degree of channeling in each core throughout MICP injection.

2.6. Calcium Mass Balance. During the four mineralization phases, the effluent was collected in batches of three pore volumes each for a total of four batches per mineralization phase. The effluent was immediately diluted by a factor of 100 and acidified to a pH of ∼1.0 using 10% nitric acid. Dissolved calcium quantification was performed via inductively coupled plasma mass spectrometry (ICP–MS), using the influent mineralization medium as a reference.

https://doi.org/10.1021/acsearthspacechem.3c00337
ACS Earth Space Chem. 2024, 8, 575–585

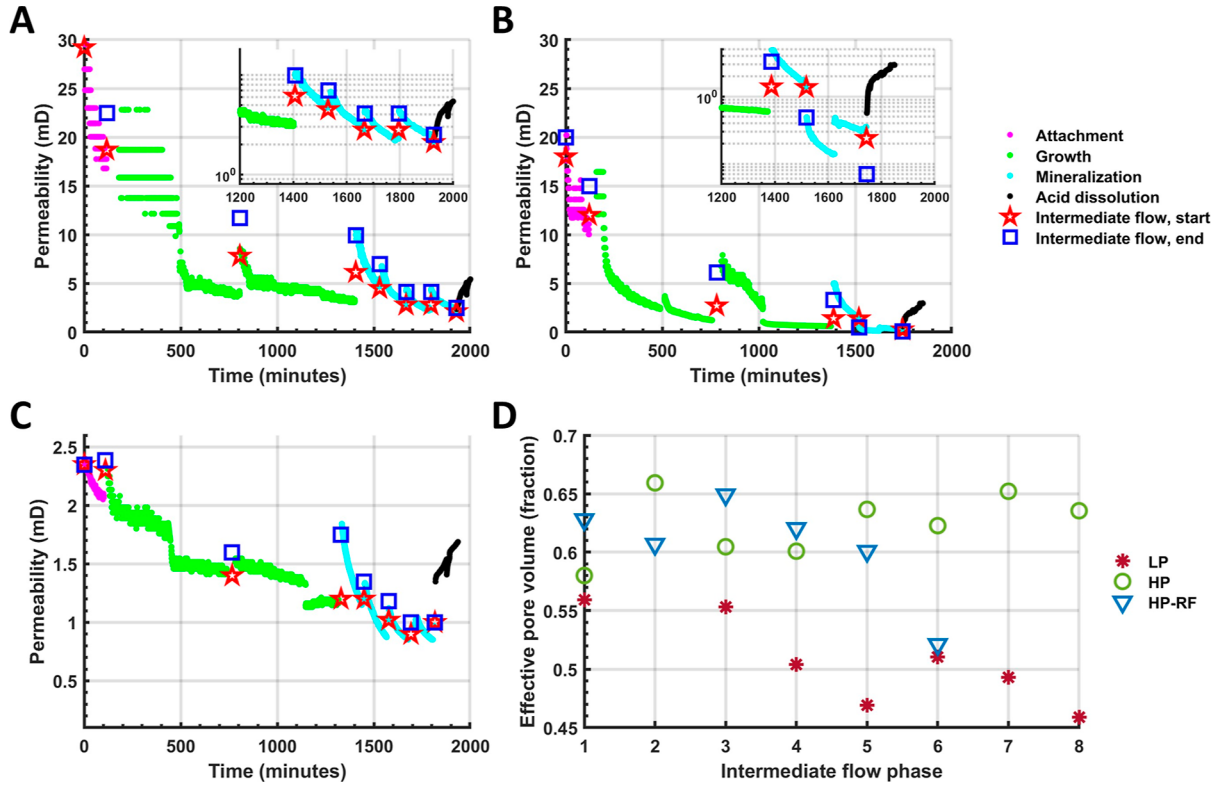

Figure 3. Real-time permeability measurements during MICP injections and subsequent acid flow for HP (A), HP-RF (B), and LP (C). Note the different *y*-axis scale for LP. (D) Effective pore volume, estimated as a fraction of gravimetrically measured pore volume from two tracer tests per intermediate flow phase. Numbered intermediate flow phases correspond to the following points in the injection: (#1) pre-MICP, (#2) post-attachment, (#3) post-growth phase 1, (#4) post-growth phase 2, (#5) post-mineralization phase 1, (#6) post-mineralization phase 2, (#7) post-mineralization phase 3, and (#8) post-mineralization phase 4. Note that the final two intermediate flow phases (#7 and #8) were not conducted for HP-RF as this injection was stopped early, and a post-attachment tracer test (#2) is not reported for LP due to a chloride electrode error.

3. RESULTS AND DISCUSSION

3.1. Initial XCT-Resolved Porosity and Pore Size Distribution. The initial porosity and pore size distribution in the four sections of each core, as estimated from XCT, are summarized and compared to the gravimetrically determined porosity in Figure 2. Although this voxel resolution fails to capture a significant fraction of the gravimetrically determined pore space (Figure 2A), the largest pores are expected to dominate flow. Additionally, given that single *S. pasteurii* cells are 1−5 μm in size and flocs may be as large as ∼100 μm,[38] nanopores and small micropores are not expected to undergo significant change during MICP. Pores of 1−15 μm will likely be clogged by physical straining of cells or small flocs, which may reduce permeability but is distinct from the attachment−growth−mineralization process studied here.

Initial porosity appears relatively uniform along the length of HP and HP-RF (Figure 2A). Analyses of the XCT-resolved pore size distribution reveal similar, relatively homogeneous pore size distributions in HP and HP-RF (Figure 2B), and distributions remain uniform along the length of each core (Figure 2D). In contrast, LP shows a smaller average pore size (Figure 2B) but greater share of large (>∼ 0.2 mm^2) pores, a pattern which is particularly pronounced near the inlet (Figure 2C). This is the expected and intended effect of using acid flow to increase the permeability and degree of channeling of the LP core.[47,50]

Experimental studies of the relationship between pore size and maximum pore-scale velocity have proposed the following power law relation between maximum velocity and pore radius[55]

$$v_m = v_0\left(r_p/r_0\right)^{\propto},\ -2 \le \propto \le 2 \quad (2)$$

Here, r_0 and v_0 represent, respectively, the characteristic pore radius and velocity, r_p represents the pore radius, and $\propto$ is a parameter that varies from −2 for a completely serial pore arrangement to +2 for a completely parallel pore arrangement. Since "serial" and "parallel" represent two theoretical extremes in how flow paths might be arranged, neither is expected to actually occur in the natural samples used here. Rather, eq 2 implies a qualitative difference in where the highest pore-scale velocities may occur in LP versus HP and HP-RF. Due to the wide range of pore sizes in LP (Figure 2C), a small number of preferential flow paths likely serve as conduits for the majority of fluid flow,[56,57] just as flow is unevenly distributed between the various possible paths in a parallel pore arrangement. HP and HP-RF, in contrast, likely feature a large number of equally likely flow paths, suggesting a more connected pore network in which most pores support similar amounts of fluid flow, as in a serial pore arrangement. Therefore, the highest flow rates are expected to occur in the preferential flow paths of LP and the narrower channels of HP and HP-RF.

3.2. Evolution of Permeability and Effective Pore Volume. Real-time permeability estimation (Figure 3) reveals several general trends that apply across the samples. First, much of the observed permeability reduction was attributable to biomass accumulation only, occurring before the injection of

https://doi.org/10.1021/acsearthspacechem.3c00337
ACS Earth Space Chem. 2024, 8, 575−585

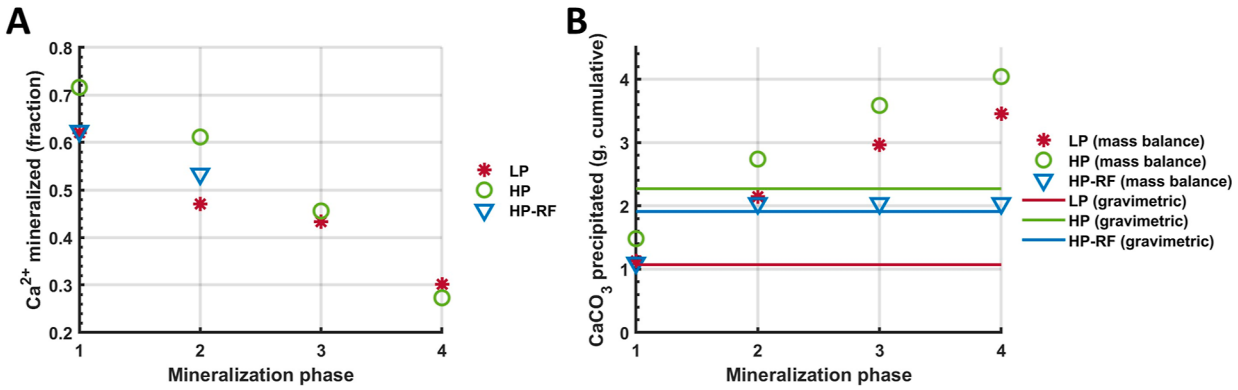

Figure 4. Fraction of dissolved calcium mineralized during each phase (A) and cumulative estimated precipitate mass, calculated from the mass balance, compared to measured change in core mass post-MICP (B).

the calcium-enriched mineralization medium ("attachment" and "growth" phases on Figure 3A–C). Second, the first growth phase produces a higher percent reduction in permeability than does the second. This is despite the fact that the quantity of biomass present in the core is expected to be greater at the beginning of the second growth phase than the first and should therefore drive more robust biomass accumulation. One possible explanation for this discrepancy is that flow-induced shear stress becomes more significant as more biomass accumulates, eventually outpacing growth. Finally, intermediate flow phases consistently yield permeability increases (compare "intermediate flow, start" and "intermediate flow, end" on Figure 3A–C), which is consistent with the mobilization and transport out of the core of biomass and precipitates under elevated flow conditions.

Outside the consistent trends noted above, the applied injection strategy was found to affect the overall permeability of the three cores in different ways. Specifically, the permeability of LP decreased only modestly, from ∼2.5 to ∼1 mD at the end of the injection (Figure 3C), while the permeability of HP-RF decreased by 3 orders of magnitude, from ∼20 to ∼0.06 mD (Figure 3B, inset plot). Permeability reduction in HP was between these two extremes, decreasing 1 order of magnitude from ∼30 to ∼2.5 mD (Figure 3A), and followed a consistent pattern of controlled decrease during injection phases and partial recovery during the intervening elevated flow phases.

The differential success of permeability reduction between LP and HP is consistent with the hypothesized prevalence of preferential flow paths in LP. The effective pore volume, estimated here through tracer test data (Figure 3D), captures the fraction of the pore space actively utilized in fluid flow. In general, a low fraction implies that many pores are too small or unconnected to serve as effective flow conduits and that flow is therefore channeled into a small number of preferential flow paths. The effective pore volume of LP and HP diverged progressively throughout the injection, with LP becoming more channeled and HP becoming less channeled. This trend may be attributable to elevated flow rates in the preferential flow paths of LP limiting biomass and precipitate accumulation. In other words, the most important flow conduits were minimally affected in LP, while the opposite seems to have occurred in HP.

In the case of HP-RF, a sudden sloughing event occurred during the rapid flow period, which followed the second mineralization phase (Figure 3B, inset plot). This is evidenced by a sudden drop in permeability of more than 1 order of magnitude in contrast to the permeability increases observed during all intermediate flow phases for HP (Figure 3A, inset plot). As a result, the planned injection schedule was cut short in HP-RF due to the pressure limits of the apparatus. Flowing more than 50 pore volumes of sodium chloride solution over 30 h failed to increase the permeability, suggesting clogging by rigid precipitate fragments too large to be transported out of the core. While such precipitate sloughing provides a means to reduce permeability quickly, the small quantity of precipitate is not expected to be resilient to subsequent acid challenges.

This intuition was confirmed by a rapid permeability increase in the early stages of the HP-RF acid challenge, with the permeabilities of HP and HP-RF eventually stabilizing to within the same order of magnitude (∼2–5 mD) (Figure 3A,B). In LP, the measured permeability at the beginning of acid flow did not correspond to the measured permeability at the end of the MICP injection (Figure 3C); this may be due to additional, unintentional clearing of precipitates and biomass during the drying and re-saturation process. However, the core also fractured at an unknown point during the acid flow procedure, confounding interpretation of these permeability measurements.

3.3. Calcium Mineralization and Mass Balance. Figure 4 summarizes the ICP–MS analyses of dissolved calcium in the effluent obtained from each mineralization phase. Based on the documented influence of biomass encapsulation by precipitated calcium carbonate,[58,59] mineralization activity is expected to decline in later mineralization phases due to inactivation of biomass and/or constraints on solute transport. While this trend is observed in Figure 4A, the amount of calcium mineralized never declines to zero, remaining at ∼30% even after the fourth mineralization phase. Such a significant level of mineralization activity is somewhat unexpected in the third and fourth phases, given that no permanent reduction in permeability occurred during these phases of mineralization for HP or LP (Figure 3A,C). This raises the question of where the presumed precipitation occurred and why it had a limited effect on permeability during the latter half of mineralization.

In Figure 4B, a mass balance of calcium is converted to a cumulative predicted mass of calcium carbonate generated throughout the four phases of mineralization, and these values are compared to the observed increase in core mass following MICP. This comparison reveals that a significant quantity of the precipitate in HP and LP was ultimately not retained within these cores after mineralization ended. In contrast, the

https://doi.org/10.1021/acsearthspacechem.3c00337
ACS Earth Space Chem. 2024, 8, 575–585

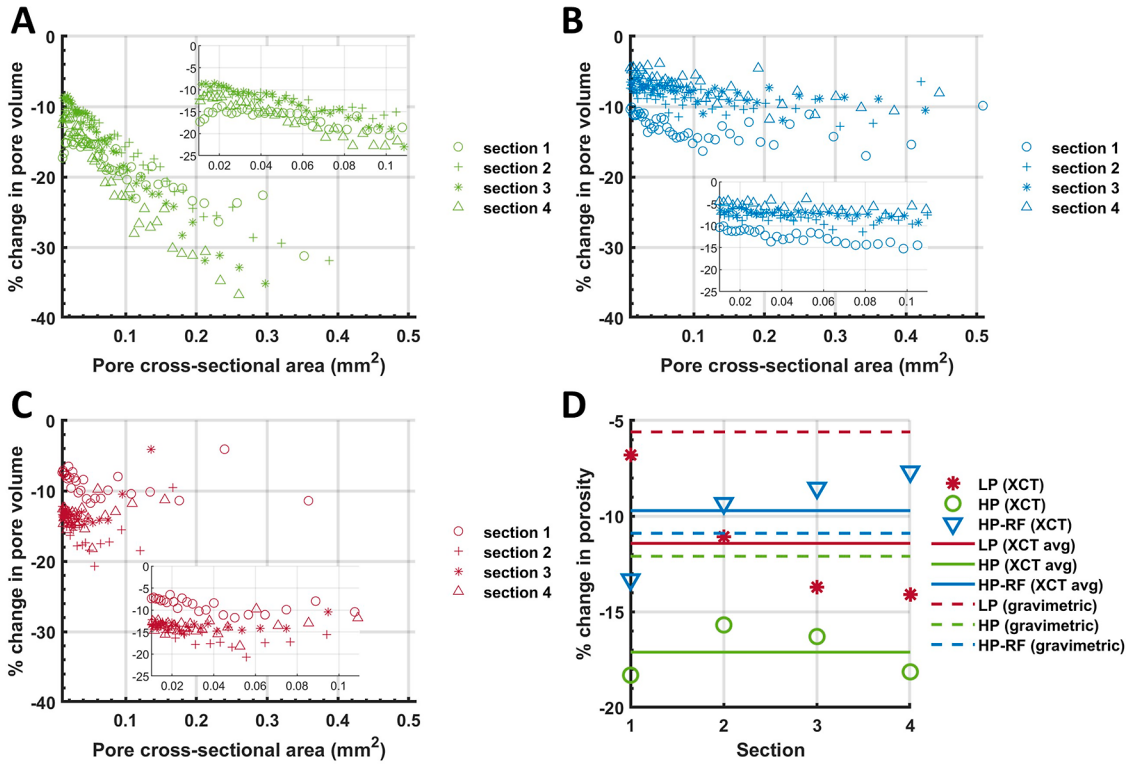

Figure 5. Percent change in pore volume within each pore size bin for HP (A), HP-RF (B), and LP (C). (D) Percent change in total XCT-resolved porosity along the four sections of each core, compared to the whole-core average and gravimetrically determined percent change in porosity.

calcium mass balance for HP-RF, which underwent only two mineralization phases, agreed well with the measured mass increase.

A likely explanation for the observed discrepancies is that intermediate flow periods induce the mobilization of precipitate masses small enough to exit the core without detectable clogging. Though precipitates are likely more resilient to shear than biomass alone, it is conceivable that there is an analogous "threshold" shear stress at which precipitate sloughing begins to occur. Since the mineralization medium contains the necessary nutrients for biomass growth, attached biomass that was previously encapsulated could be re-exposed during precipitate sloughing and resume normal metabolic activity; this would explain higher-than-expected mineralization activity in later mineralization phases. Shear limitations would continue to apply, however, creating a dynamic process of sloughing during intermediate flow followed by re-encapsulation during mineralization medium injection.

The above interpretation assumes that precipitation originates primarily from the attached biomass. This assumption is commonly applied to modeled MICP processes.[19,22,23] While the methods used in this study do not provide evidence for or against a suspended biomass contribution to precipitate accumulation, such a contribution would not be at odds with the data presented here. In an alternative scenario where surface-attached precipitates are immobile and not subject to shear sloughing, incomplete retention of precipitates could be explained by biomass–precipitate colloids that settle on pore surfaces during slow flow and are washed out during faster flow. Provided that sufficient active biomass remained in the core at the start of each mineralization phase, simultaneous growth and precipitation would produce a repeating pattern of colloid settling and washout that would mimic the proposed encapsulation–sloughing cycle.

3.4. Precipitate Accumulation in Differently Sized Pores. Figure 5 summarizes the XCT-resolved changes in porosity that occurred following MICP as functions of both the pore size (Figure 5A–C) and core section (Figure 5D), with Section 1 being closest to the core inlet and Section 4 being closest to the core outlet. As Figure 5A shows, the percent change in the pore volume is directly proportional to the pore size. In other words, for the HP core, precipitate accumulation occurred preferentially in larger pores. In contrast, HP-RF (Figure 5B) shows less precipitate accumulation across all size ranges compared with HP, and the relationship between size and percent change in pore volume is weaker. For LP (Figure 5C), there may be a similar proportionality between pore size and percent change in pore volume for the smallest pore size fraction, but the trend reverses at larger pore sizes, which likely represent preferential flow paths. It is also important to note that precipitate accumulation favors the inlet in HP-RF and the outlet in LP, while no trend from the inlet to outlet can be discerned in HP (Figure 5D).

These observations are consistent with the patterns of precipitate accumulation and mobilization previously hypothesized for the three samples. Due to the absence of preferential flow paths in HP (Figure 2), the highest velocities and greatest shear stresses likely occur in small pores (eq 2). Favorable conditions for precipitate accumulation in large pores prevent flow in HP from becoming more channeled as the injection proceeds (Figure 3D); this is in sharp contrast to LP, where elevated flow rates in larger pores may cause preferential flow paths to remain open, and as a result, only a modest decrease in permeability is observed (Figure 3C). Furthermore, the acid

https://doi.org/10.1021/acsearthspacechem.3c00337
ACS Earth Space Chem. 2024, 8, 575–585

dissolution method applied to the LP core likely resulted in more significant channeling near the inlet (Figure 2A,C), which could explain increasing precipitate accumulation with a greater distance from the inlet.

Since the HP-RF injection could not proceed beyond mineralization phase #2 of 4, more precipitate accumulation near the inlet of this core is not surprising. Dissolved calcium concentrations in the mineralization medium are expected to be highest near the inlet, and the rate of precipitation should accordingly decrease along the length of the core. As a result, it is likely near the inlet that precipitate accumulation first reaches the maximum allowable by encapsulation or flow-induced shear stress. Had the injection proceeded in HP-RF, the amount of precipitate in Sections 2−4 may have more closely matched the amount in Section 1. Regardless, the permeability decrease was larger in HP-RF than HP (Figure 3) despite a smaller quantity of precipitate overall (Figure 4), since the dominant process in HP-RF was clogging by sloughed precipitates rather than gradual shrinking of all pores.

4. SUMMARY AND CONCLUSIONS

This study assessed the potential for flow-induced bulk transport of biomass and precipitates to either limit or enhance the permeability reduction achieved during a staged, continuous-flow, bioaugmented MICP injection. When flow rates are moderate and flow is distributed across many flow paths, precipitate accumulation is uniform along the length of the core and occurs preferentially in large pores, so that the degree of channeling does not increase. Under such conditions, consecutive injections could theoretically be applied to achieve tunable permeability reduction, even when the average pore size is large. Elevated flow rates did not significantly suppress biomass or precipitate accumulation but did induce sloughing and mobilization of precipitates. Such sloughing events lead to clogging, which produces a large and sudden reduction in the permeability. Permeability recovers quickly, however, when the seal is challenged with an acid. Upon moving from a homogeneous pore size distribution to a more heterogeneous one, preferential flow paths pose a challenge for robust permeability reduction, with flow-induced shear stresses predicted to limit the accumulation of both biomass and precipitates.

Taken together, these findings suggest that flow-induced shear stress, itself a product of Darcy velocity and the initial size and arrangement of pores, may be as important as biological and chemical factors in determining the permeability reduction achievable by MICP. While the natural samples used here provide valuable qualitative insights into scenarios that may be encountered in a real reservoir, studies of more controlled systems are necessary to answer several lingering questions. First, since the hypothesized contributions of biomass and precipitate mobilization could not be decoupled in this study, these processes should be studied separately with an emphasis on relating pore-scale flow velocity to sloughing behavior. Second, a more complete understanding is needed of the biological factors that might affect the resilience of attached *S. pasteurii* to high-shear conditions, such as biofilm morphology, EPS production, and rheotaxis-mediated reattachment of sloughed biomass. Finally, while this study proposes that precipitate sloughing is ubiquitous and causes detectable clogging only under certain conditions, quantitative characterization of unknowns, including the size and morphology of sloughed precipitates and prevalence of precipitates formed by suspended biomass, is necessary to refine MICP models accordingly.

■ ASSOCIATED CONTENT

Supporting Information

The Supporting Information is available free of charge at https://pubs.acs.org/doi/10.1021/acsearthspacechem.3c00337.

Additional experimental details, raw data, and code used for analysis of pore size distribution (PDF)

■ AUTHOR INFORMATION

Corresponding Author

Brian R. Ellis − *Civil and Environmental Engineering, University of Michigan, Ann Arbor, Michigan 48109, United States;* orcid.org/0000-0002-7253-4285; Email: brellis@umich.edu

Author

Eva M. Albalghiti − *Civil and Environmental Engineering, University of Michigan, Ann Arbor, Michigan 48109, United States*

Complete contact information is available at: https://pubs.acs.org/10.1021/acsearthspacechem.3c00337

Notes

The authors declare no competing financial interest.

■ ACKNOWLEDGMENTS

All X-ray computed tomography data were gathered in the CTEES facility at University of Michigan, supported by the Department of Earth and Environmental Sciences and College of Literature, Sciences, and the Arts. This study is based upon work supported by the National Science Foundation (CAREER Grant 1943726) and the Alfred P. Sloan Foundation (Grant 2020-12466).

■ REFERENCES

(1) Fujita, Y.; Ferris, F. G.; Lawson, R. D.; Colwell, F. S.; Smith, R. W. Subscribed Content Calcium Carbonate Precipitation by Ureolytic Subsurface Bacteria. *Geomicrobiol. J.* **2000**, *17* (4), 305−318.

(2) Ferris, F. G.; Phoenix, V.; Fujita, Y.; Smith, R. W. Kinetics of calcite precipitation induced by ureolytic bacteria at 10 to 20°C in artificial groundwater. *Geochim. Cosmochim. Acta* **2004**, *68* (8), 1701−1710.

(3) Mitchell, A. C.; Ferris, F. G. The Influence of Bacillus Pasteurii on the Nucleation and Growth of Calcium Carbonate. *Geomicrobiol. J.* **2006**, *23* (3−4), 213−226.

(4) Whiffin, V. S.; van Paassen, L. A.; Harkes, M. P. Microbial Carbonate Precipitation as a Soil Improvement Technique. *Geomicrobiol. J.* **2007**, *24* (5), 417−423.

(5) Lauchnor, E. G.; Schultz, L. N.; Bugni, S.; Mitchell, A. C.; Cunningham, A. B.; Gerlach, R. Bacterially Induced Calcium Carbonate Precipitation and Strontium Coprecipitation in a Porous Media Flow System. *Environ. Sci. Technol.* **2013**, *47* (3), 1557−1564.

(6) Mitchell, A. C.; Dideriksen, K.; Spangler, L. H.; Cunningham, A. B.; Gerlach, R. Microbially Enhanced Carbon Capture and Storage by Mineral-Trapping and Solubility-Trapping. *Environ. Sci. Technol.* **2010**, *44*, 5270−5276.

(7) Cunningham, A. B.; Phillips, A. J.; Troyer, E.; Lauchnor, E.; Hiebert, R.; Gerlach, R.; Spangler, L. Wellbore Leakage Mitigation Using Engineered Biomineralization. *Energy Procedia* **2014**, *63*, 4612−4619.

(8) Phillips, A. J.; Troyer, E.; Hiebert, R.; Kirkland, C.; Gerlach, R.; Cunningham, A. B.; Spangler, L.; Kirksey, J.; Rowe, W.; Esposito, R. Enhancing Wellbore Cement Integrity with Microbially Induced Calcite Precipitation (MICP): A Field Scale Demonstration. *J. Pet. Sci. Eng.* **2018**, *171*, 1141−1148.
(9) Kirkland, C. M.; Norton, D.; Firth, O.; Eldring, J.; Cunningham, A. B.; Gerlach, R.; Phillips, A. J. Visualizing MICP with X-Ray M-CT to Enhance Cement Defect Sealing. *Int. J. Greenhouse Gas Control* **2019**, *86*, 93−100.
(10) Kirkland, C. M.; Thane, A.; Hiebert, R.; Hyatt, R.; Kirksey, J.; Cunningham, A. B.; Gerlach, R.; Spangler, L.; Phillips, A. J. Addressing Wellbore Integrity and Thief Zone Permeability Using Microbially-Induced Calcium Carbonate Precipitation (MICP): A Field Demonstration. *J. Pet. Sci. Eng.* **2020**, *190*, 107060.
(11) Kirkland, C. M.; Hiebert, R.; Hyatt, R.; McCloskey, J.; Kirksey, J.; Thane, A.; Cunningham, A. B.; Gerlach, R.; Spangler, L.; Phillips, A. J. Direct Injection of Biomineralizing Agents to Restore Injectivity and Wellbore Integrity. *SPE Prod. Oper.* **2021**, *36* (01), 216−223.
(12) Phillips, A. J.; Cunningham, A. B.; Gerlach, R.; Hiebert, R.; Hwang, C.; Lomans, B. P.; Westrich, J.; Mantilla, C.; Kirksey, J.; Esposito, R.; Spangler, L. Fracture Sealing with Microbially-Induced Calcium Carbonate Precipitation: A Field Study. *Environ. Sci. Technol.* **2016**, *50* (7), 4111−4117.
(13) DeJong, J.; Gomez, M.; San Pablo, A.; Graddy, C.; Nelson, D.; Lee, M.; Ziotopoulou, K.; El Kortbawi, M.; Montoya, B.; Kwon, T. State of the Art: MICP Soil Improvement and Its Application to Liquefaction Hazard Mitigation. In *Proceedings of the 20th ICSMGE-State of the Art and Invited Lectures*; National Science Foundation, 2022.
(14) Graddy, C. M.; Gomez, M. G.; Kline, L. M.; Morrill, S. R.; DeJong, J. T.; Nelson, D. C. Diversity of Sporosarcina-like Bacterial Strains Obtained from Meter-Scale Augmented and Stimulated Biocementation Experiments. *Environ. Sci. Technol.* **2018**, *52* (7), 3997−4005.
(15) Graddy, C. M.; Gomez, M. G.; DeJong, J. T.; Nelson, D. C. Native Bacterial Community Convergence in Augmented and Stimulated Ureolytic MICP Biocementation. *Environ. Sci. Technol.* **2021**, *55* (15), 10784−10793.
(16) Tobler, D. J.; Cuthbert, M. O.; Greswell, R. B.; Riley, M. S.; Renshaw, J. C.; Handley-Sidhu, S.; Phoenix, V. R. Comparison of Rates of Ureolysis between Sporosarcina Pasteurii and an Indigenous Groundwater Community under Conditions Required to Precipitate Large Volumes of Calcite. *Geochim. Cosmochim. Acta* **2011**, *75* (11), 3290−3301.
(17) Cuthbert, M. O.; McMillan, L. A.; Handley-Sidhu, S.; Riley, M. S.; Tobler, D. J.; Phoenix, V. R. A Field and Modeling Study of Fractured Rock Permeability Reduction Using Microbially Induced Calcite Precipitation. *Environ. Sci. Technol.* **2013**, *47* (23), 13637−13643.
(18) Landa-Marbán, D.; Tveit, S.; Kumar, K.; Gasda, S. E. Practical Approaches to Study Microbially Induced Calcite Precipitation at the Field Scale. *Int. J. Greenhouse Gas Control* **2020**, *106*, 103256.
(19) Hommel, J.; Lauchnor, E.; Gerlach, R.; Cunningham, A. B.; Ebigbo, A.; Helmig, R.; Class, H. Investigating the Influence of the Initial Biomass Distribution and Injection Strategies on Biofilm-Mediated Calcite Precipitation in Porous Media. *Transp. Porous Media* **2016**, *114* (2), 557−579.
(20) Tobler, D. J.; Maclachlan, E.; Phoenix, V. R. Microbially Mediated Plugging of Porous Media and the Impact of Differing Injection Strategies. *Ecol. Eng.* **2012**, *42*, 270−278.
(21) Zambare, N. M.; Lauchnor, E. G.; Gerlach, R. Controlling the Distribution of Microbially Precipitated Calcium Carbonate in Radial Flow Environments. *Environ. Sci. Technol.* **2019**, *53* (10), 5916−5925.
(22) Ebigbo, A.; Phillips, A.; Gerlach, R.; Helmig, R.; Cunningham, A. B.; Class, H.; Spangler, L. H. Darcy-Scale Modeling of Microbially Induced Carbonate Mineral Precipitation in Sand Columns. *Water Resour. Res.* **2012**, *48* (7), W07519.
(23) Cunningham, A. B.; Class, H.; Ebigbo, A.; Gerlach, R.; Phillips, A. J.; Hommel, J. Field-Scale Modeling of Microbially Induced Calcite Precipitation. *Comput. Geosci.* **2019**, *23* (2), 399−414.
(24) Minto, J. M.; El Mountassir, G.; Lunn, R. J. Micro-Continuum Modelling of Injection Strategies for Microbially Induced Carbonate Precipitation. *E3S Web Conf.* **2019**, *92*, 11019.
(25) Minto, J. M.; Lunn, R. J.; El Mountassir, G. Development of a Reactive Transport Model for Field-Scale Simulation of Microbially Induced Carbonate Precipitation. *Water Resour. Res.* **2019**, *55* (8), 7229−7245.
(26) Aufrecht, J. A.; Fowlkes, J. D.; Bible, A. N.; Morrell-Falvey, J.; Doktycz, M. J.; Retterer, S. T. Pore-Scale Hydrodynamics Influence the Spatial Evolution of Bacterial Biofilms in a Microfluidic Porous Network. *PLoS One* **2019**, *14* (6), No. e0218316.
(27) Scheibe, T. D.; Dong, H.; Xie, Y. Correlation between Bacterial Attachment Rate Coefficients and Hydraulic Conductivity and Its Effect on Field-Scale Bacterial Transport. *Biol. Process. Porous Media Pore Scale Field* **2007**, *30* (6−7), 1571−1582.
(28) Secchi, E.; Vitale, A.; Miño, G. L.; Kantsler, V.; Eberl, L.; Rusconi, R.; Stocker, R. The Effect of Flow on Swimming Bacteria Controls the Initial Colonization of Curved Surfaces. *Nat. Commun.* **2020**, *11* (1), 2851.
(29) Carrel, M.; Morales, V. L.; Beltran, M. A.; Derlon, N.; Kaufmann, R.; Morgenroth, E.; Holzner, M. Biofilms in 3D Porous Media: Delineating the Influence of the Pore Network Geometry, Flow and Mass Transfer on Biofilm Development. *Water Res.* **2018**, *134*, 280−291.
(30) Kurz, D. L.; Secchi, E.; Carrillo, F. J.; Bourg, I. C.; Stocker, R.; Jimenez-Martinez, J. Competition between Growth and Shear Stress Drives Intermittency in Preferential Flow Paths in Porous Medium Biofilms. *Proc. Natl. Acad. Sci. U.S.A.* **2022**, *119* (30), No. e2122202119.
(31) Liu, N.; Skauge, T.; Landa-Marbán, D.; Hovland, B.; Thorbjørnsen, B.; Radu, F. A.; Vik, B. F.; Baumann, T.; Bødtker, G. Microfluidic Study of Effects of Flow Velocity and Nutrient Concentration on Biofilm Accumulation and Adhesive Strength in the Flowing and No-Flowing Microchannels. *J. Ind. Microbiol. Biotechnol.* **2019**, *46* (6), 855−868.
(32) Stoodley, P.; Dodds, I.; De Beer, D.; Scott, H. L.; Boyle, J. D. Flowing Biofilms as a Transport Mechanism for Biomass through Porous Media under Laminar and Turbulent Conditions in a Laboratory Reactor System. *Biofouling* **2005**, *21* (3−4), 161−168.
(33) Rupp, C. J.; Fux, C. A.; Stoodley, P. Viscoelasticity of Staphylococcus Aureus Biofilms in Response to Fluid Shear Allows Resistance to Detachment and Facilitates Rolling Migration. *Appl. Environ. Microbiol.* **2005**, *71* (4), 2175−2178.
(34) Sharp, R. R.; Stoodley, P.; Adgie, M.; Gerlach, R.; Cunningham, A. Visualization and Characterization of Dynamic Patterns of Flow, Growth and Activity of Biofilms Growing in Porous Media. *Water Sci. Technol.* **2005**, *52* (7), 85−90.
(35) Geisel, S.; Secchi, E.; Vermant, J. The Role of Surface Adhesion on the Macroscopic Wrinkling of Biofilms. *eLife* **2022**, *11*, No. e76027.
(36) Ebigbo, A.; Helmig, R.; Cunningham, A. B.; Class, H.; Gerlach, R. Modelling Biofilm Growth in the Presence of Carbon Dioxide and Water Flow in the Subsurface. *Adv. Water Resour.* **2010**, *33* (7), 762−781.
(37) Armstrong, R.; Ajo-Franklin, J. Investigating Biomineralization Using Synchrotron Based X-Ray Computed Microtomography. *Geophys. Res. Lett.* **2011**, *38* (8), L08406.
(38) Mountassir, G. E.; Lunn, R. J.; Moir, H.; MacLachlan, E. Hydrodynamic Coupling in Microbially Mediated Fracture Mineralization: Formation of Self-Organized Groundwater Flow Channels. *Water Resour. Res.* **2014**, *50* (1), 1−16.
(39) Ribeiro, B. G. O.; Gomez, M. G. Dissolution Behavior of Ureolytic Biocementation: Physical Experiments and Reactive Transport Modeling. *J. Geotech. Geoenviron. Eng.* **2023**, *149* (9), 04023071.
(40) Sang, G.; Lunn, R. J.; El Mountassir, G.; Minto, J. M. Transport and Fate of Ureolytic Sporosarcina Pasteurii in Saturated Sand

Columns: Experiments and Modelling. *Transp. Porous Media* **2023**, *149*, 599−624.
(41) Zhong, M.; Liu, B.; Chen, J.; Yan, G. Research on Plugging Characteristics of Microorganism Induced Calcite Precipitation in Sandstone Environment. *J. Pet. Sci. Eng.* **2022**, *218*, 111040.
(42) Tobler, D. J.; Cuthbert, M. O.; Phoenix, V. R. Transport of Sporosarcina Pasteurii in Sandstone and Its Significance for Subsurface Engineering Technologies. *Appl. Geochem.* **2014**, *42*, 38−44.
(43) Song, C.; Elsworth, D.; Jia, Y.; Lin, J. Permeable Rock Matrix Sealed with Microbially-Induced Calcium Carbonate Precipitation: Evolutions of Mechanical Behaviors and Associated Microstructure. *Eng. Geol.* **2022**, *304*, 106697.
(44) Minto, J. M.; Hingerl, F. F.; Benson, S. M.; Lunn, R. J. X-Ray CT and Multiphase Flow Characterization of a 'Bio-Grouted' Sandstone Core: The Effect of Dissolution on Seal Longevity. *Int. J. Greenhouse Gas Control* **2017**, *64*, 152−162.
(45) Hommel, J.; Cunningham, A. B.; Helmig, R.; Ebigbo, A.; Class, H. Numerical Investigation of Microbially Induced Calcite Precipitation as a Leakage Mitigation Technology. *Energy Procedia* **2013**, *40*, 392−397.
(46) Geindreau, C.; Emeriault, F.; Dadda, A.; Yaba, O.; Spadini, L.; Esnault Filet, A.; Garandet, A. Mechanical and Microstructural Changes of Biocemented Sand Subjected to an Acid Solution. *Int. J. GeoMech.* **2022**, *22* (3), 04021307.
(47) Xiao, T.; Kweon, H.; McPherson, B.; Deo, M. Wormhole Generations in Indiana Limestone with CO2 Intrusion: Numerical Simulations Based on Core Flooding Experiments. *Energy Fuels* **2017**, *31* (11), 12487−12499.
(48) Rodriguez-Navarro, C.; Jroundi, F.; Schiro, M.; Ruiz-Agudo, E.; González-Muñoz, M. T. Influence of Substrate Mineralogy on Bacterial Mineralization of Calcium Carbonate: Implications for Stone Conservation. *Appl. Environ. Microbiol.* **2012**, *78* (11), 4017−4029.
(49) Liu, J.; Polak, A.; Elsworth, D.; Grader, A. Dissolution-Induced Preferential Flow in a Limestone Fracture. *J. Contam. Hydrol.* **2005**, *78* (1−2), 53−70.
(50) Voltolini, M.; Ajo-Franklin, J. The Effect of CO2-Induced Dissolution on Flow Properties in Indiana Limestone: An in Situ Synchrotron X-Ray Micro-Tomography Study. *Int. J. Greenhouse Gas Control* **2019**, *82*, 38−47.
(51) Thompson, E. P.; Tomenchok, K.; Olson, T.; Ellis, B. R. Reducing User Bias in X-Ray Computed Tomography-Derived Rock Parameters through Image Filtering. *Transp. Porous Media* **2021**, *140* (2), 493−509.
(52) Shook, G. M.; Ansley, S. L.; Wylie, A. *Tracers and Tracer Testing: Design, Implementation, and Interpretation Methods*; Idaho National Engineering and Environmental Laboratory Bechtel BWXT Idaho, LLC, 2004.
(53) Skauge, A.; Vik, B.; Pourmohammadi, S.; Spildo, K. *Dispersion Measurements Used in Special Core Analysis of Carbonates*, 2006, pp 12−16.
(54) Benjamin, M. M.; Lawler, D. F. *Water Quality Engineering: Physical/Chemical Treatment Processes*; Wiley: Hoboken, NJ, 2013.
(55) Holzner, M.; Morales, V. L.; Willmann, M.; Dentz, M. Intermittent Lagrangian Velocities and Accelerations in Three-Dimensional Porous Medium Flow. *Phys. Rev. E* **2015**, *92* (1), 013015.
(56) Bianchi, M.; Zheng, C.; Wilson, C.; Tick, G. R.; Liu, G.; Gorelick, S. M. Spatial Connectivity in a Highly Heterogeneous Aquifer: From Cores to Preferential Flow Paths. *Water Resour. Res.* **2011**, *47* (5), W05524.
(57) Moreno, L.; Tsang, C.-F. Flow Channeling in Strongly Heterogeneous Porous Media: A Numerical Study. *Water Resour. Res.* **1994**, *30* (5), 1421−1430.
(58) Cuthbert, M. O.; Riley, M. S.; Handley-Sidhu, S.; Renshaw, J. C.; Tobler, D. J.; Phoenix, V. R.; Mackay, R. Controls on the Rate of Ureolysis and the Morphology of Carbonate Precipitated by S. Pasteurii Biofilms and Limits Due to Bacterial Encapsulation. *Ecol. Eng.* **2012**, *41*, 32−40.
(59) Zambare, N. M.; Naser, N. Y.; Gerlach, R.; Chang, C. B. Mineralogy of Microbially Induced Calcium Carbonate Precipitates Formed Using Single Cell Drop-Based Microfluidics. *Sci. Rep.* **2020**, *10* (1), 17535.

https://doi.org/10.1021/acsearthspacechem.3c00337
ACS Earth Space Chem. 2024, 8, 575−585